Unsaturated Nd-Bi dual-metal sites enable efficient NIR light-driven O₂ activation for water purification

Qiuwen Wang [a], Dongyu Xu [a], Yilin Dong [a], Shaoxuan Pang [a], Lijun Zhang [a], Guangming Zhang [a], Longyi Lv [a], Xiaoyang Liu [a], Yuguo Xia [b], Luiza C Campos [c], Zhijun Ren [a*], Pengfei Wang [a*]

[a] Tianjin Key Laboratory of Clean Energy and Pollutant Control, School of Energy and Environmental Engineering, Hebei University of Technology, Tianjin 300401, China

[b] School of Chemistry and Chemical Engineering, National Engineering Research Center for Colloidal Materials, Shandong University, Jinan 250100, China

[c] Department of Civil, Environmental and Geomatic Engineering, University College London, London WC1E 6BT, United Kingdom

*Correspondence to: Z. J. Ren (E-mail: renzhijun2003@126.com) & P. F. Wang (E-mail: pengfeiwang@hebut.edu.cn)

Abstract

Metal semiconductor catalysts with oxygen vacancies can make full use of near infrared light to active O_2 for degradation of emerging pollutants. However, the surface oxygen vacancies can also become the combination center of electron-hole pairs, leading O_2 cannot accept more electrons for activation, often becoming the bottleneck. In this study, by doping half-metal BiO_{2-x} with Nd to form unsaturated Nd-Bi dual-metal sites as oxygen chemisorption and electron transfer sites, this bottleneck can be well solved. Systematic characterization results imply that Nd-Bi dual-metal sites can raise the center of the defect band to the Fermi level, which preserves the energy of photoexcited electrons. Thus, more electrons are driven to adsorbates for $O_2^{\cdot-}$ generation. Under liquid phase determination conditions, the modified sample achieves the reaction-rate constant for doxycycline degradation of 134.4×10^{-4} min^{-1}, which is about 24.2 times higher than that of pristine BiO_{2-x} under NIR irradiation.

Keywords: Nd-Bi dual-metal sites, Photocatalysis, Molecular oxygen activation, NIR light, Emerging organic pollutants

1. Introduction

Emerging organic pollutants (EOCs) are some artificial organic substances that do not exist in the natural environment, and are usually detected in the concentration of ng/L and μg/L in polluted water, causing the greatest damage to the ecosystem [1-2]. Pharmaceutical is a subclass of EOCs and antibiotics are regarded as representative substances because of their great contribution to human and animal medicine. Antibiotics take an important effect in derivation and transmission of antibiotic resistance genes (ARGs) in water, and have become a major environmental problem in recent years [3-4]. Therefore, it is epochmaking to develop effective technology to eliminate completely antibiotics in water, and in recent years, advanced oxidation processes (AOPs) method has been applied to resolve the problem of antibiotic contamination. Among AOPs technologies, photocatalytic molecular oxygen (O_2) activation has been deemed as up-and-coming technology for antibiotic degradation due to its simplicity and high efficiency [5-6]. Through photogenerated electrons action, it can promote the O_2 adsorbed on the surface of catalysts to reactive oxygen species (ROS), such as hydrogen peroxide (H_2O_2), hydroxyl radical ($\cdot OH$), superoxide anion radical ($O_2^{\cdot-}$) and singlet oxygen ($^1O_2$). The ROS has strong oxidation capacity and can degrade antibiotics in water to achieve water purification [7]. Some semiconductor materials are being studied by researchers, such as TiO_2, C_3N_4, CeO_2, CdS and ZnO. However, all these catalysts have the characteristic of wide band gap [8-10]. In solar energy, near-infrared (NIR) light accounts for about 50%, but in fact, wide-band gap photocatalysts cannot absorb near-infrared light for effective utilization, thus limiting the utilization efficiency of solar energy. As for these issues, it is still a tremendous

challenge to seek extremely efficient photocatalysts for the degradation of antibiotics with higher utilization efficiency of solar energy and extending to the near-infrared range [11].

A typical O_2 activation in the photocatalytic reaction chiefly constitutes photoabsorption, electron-hole separation and transfer, and O_2 reduction by photoexcited electrons. Metal photocatalysts have almost no bandgaps compared to traditional semiconductor photocatalysts, so they can be excited by visible or even infrared light and solve this problem of light absorption [12]. For this matter, a cheap metallic semiconductor with narrow band gap and practical near infrared photocatalytic activity is worthy of application. Besides, the rapid reduction of O_2 on the catalyst surface is also a pivotal element affecting the activity. The common physical adsorption is difficult to provide valid channels for electron transfer from catalysts noumenon to molecules. In order to get well chemisorption of the molecule at the active site of photocatalyst, many methods have been employed, such as compound modification [13], element doping [14] and introducing defects [15]. Among them, defect engineering has attracted tremendous attention to provide coordination unsaturated sites with low valence metals for molecular chemisorption ability. The scheme creates an efficient channel for electron migrate to the adsorbed O_2 molecules [16]. However, the development of defective engineered photocatalysts is still restricted by some bottlenecks. On account of the rapid recombination rate of the photogenerated carriers at the oxygen vacancies sites, reducing the carries recombination rate and enhancing electrons transfer rate to O_2 in a photocatalytic system is still an urgent task.

Inspired by the above considerations, neodymium (Nd) doped half-metal BiO_{2-x} with a mass of oxygen vacancies is used as a representative material to settle the above matter. Multiple characterization methods and theoretical calculations indicate that the Nd species substituted Bi atoms linking oxygen vacancy can be used as the active sites for the chemisorption of O_2 molecules, at which the unsaturated Nd-Bi dual-metal sites with larger adsorption energy and provide a bridge for the migration of photoexcited electrons from the photocatalyst body to O_2 molecules, compared with unsaturated Bi-Bi single metal sites, it can promote the fast transfer of charge and increase the transfer amount, thus improving the activation efficiency (Fig. 1a). The unsaturated dual-metal sites induced by subtle Nd doping improve the photocatalytic performance of pollutant removal significantly. The Nd doped BiO_{2-x} achieves the reaction-rate constant for doxycycline degradation of 134.4×10^{-4} min^{-1}, approximately 24.2 times higher than that of BiO_{2-x} under liquid phase determination conditions.

2. Experimental section

2.1. Preparation of Nd-BiO_{2-x} photocatalyst

As schematically illustrated in Fig. S1, these samples are synthesized by a mild hydrothermal method [17]. In a preparation course, NaOH, $NaBiO_3$ and $Nd(NO_3)_3 \cdot 6H_2O$ were added into 60 mL of deionized water. Four representative doping concentrations were chosen: 2, 4, 6, and 8% (where the percent is defined as the molar percentage of doped Nd atoms). The suspended solution was decanted into 90 mL stainless steel PVP-lined autoclave after magnetic stirring for 1 h. Sealed autoclave, heated at 180°C, maintained 6 h, whereafter cooled naturally to room temperature. The

collected reactants were washed by using distilled water and dried at 80°C for 4 h. Among all the samples, the sample with 6% Nd doping appears the best activity, and it was chosen as the model catalyst in this study (marked as BO_V:Nd). Meanwhile, as a comparison, the original BiO_{2-x} was only without $Nd(NO_3)_3 \cdot 6H_2O$ (marked as BO_V).

2.2. Characterization of samples

The crystal structure of solid photocatalyst was studied by X-ray diffraction (XRD) using a Philips Xpert. The morphology feature and microstructure of the catalyst were scanned by the transmission electron microscopy (TEM, JEOL JEM-2100F). Atomic-resolution high-angle annular dark-field scanning transmission electron microscopy (HAADF-STEM) image (Titan Cubed Themis G2300) was implemented to exhibit the atomic structures. The BRUKER Dimension Icon microscope was employed to test the atomic force microscopy (AFM). The Fourier transform infrared (FTIR) spectrum was registered for the results on the FTIR spectrograph (Thermo Nicolet iS5). The Raman spectrum was implemented on a Renishaw Invia confocal Raman microscope system with charge-coupled device detector. A Thermo Fisher K-Alpha spectrometer was used to collect the X-ray photoelectron spectroscopy (XPS) to explore the surface chemical element. The electron paramagnetic resonance (EPR) spectrometer (A300-10/12, Bruker) can record the oxygen vacancy of the samples. Ultraviolet photoelectron spectroscopy (UPS, Thermo ESCALAB XI+) weas recorded with a -5 V bias. The UV-Vis spectrophotometer (UV-3600, Shimadzu) was implemented to record the UV-Vis absorption spectra of the samples. The electron spin resonance (ESR) spectrometer (A300-10/12, Bruker) was proceeded to detect the reactive oxygen species using

DMPO (5,5-dimethyl-l-pyrroline n-oxide) as a spin trap. The surface photovoltage (SPV) spectrum was noted with a IPCE1000 surface photovoltage spectroscopy (Perfect Light, Ltd). Steady-state photoluminescence (PL) spectrum of the samples were conducted on the fluorescence spectrometer FL3-22. The FLS1000 fluorescence lifetime spectrophotometer was employed to record the Time-resolved PL (TRPL) decay curves. The intermediates of doxycycline and sodium butyl xanthate degradation were implemented on liquid chromatography-mass spectrometry (LC-MS) linked an ESI source together. A method for determining the total organic carbon (TOC) was developed by total organic carbon solid sampling system TOC-L. ASAP2460 system was used for the specific surface area test through Brunauer-Emmett-Teller (BET) method.

2.3. Photocatalytic activity evaluation

The degradation effect of doxycycline in visible light ($\lambda > 420$ nm) and near infrared light ($\lambda > 800$ nm), then the photocatalytic performance of the synthesized photocatalyst was evaluated. The light source is 300 W xenon lamp by using CEL-HXF300, (Beijing zhongjiaojinyuan, China), which has 800 nm or 420 nm optical filter. Prepare 100 mL 10 mg/L DC solution and disperse the prepared 20 mg photocatalyst in it. After that, the suspension was stirred under dark conditions until the adsorption desorption equilibrium was reached. In the photocatalytic degradation process, 5 mL suspension samples were taken out (under NIR light every 20 min and visible light every 10 min) and removed through a 0.22 μm filter. Then the concentration of doxycycline was measured by High Performance Liquid Chromatography (HPLC). The composition and

proportion of mobile phase were methanol: acetonitrile: 0.010 M oxalic acid (2: 3: 5, v/v/v). At 350 nm absorption wavelength, the mobile phase was evenly pumped at 1.50 mL min^{-1}, meanwhile the injection quantity was 50 µL at 20°C. The peak area is converted into DC solution concentration by the standard curve [18]. The pseudo first-order model was used to study the photocatalytic degradation kinetics, and C/C_0 was used to calculate the degradation efficiency (where C_0 and C are the concentrations of DC in the initial value and the exact time t).

$$\ln(C/C_0) = -kt \qquad\qquad (1)$$

Among them the k represented as the apparent rate constant (min^{-1}) [19].

2.4. Theoretical calculation

The exchange correlation functions been from Perdew, Burke and Ernzerof (PBE) were calculated by employing generalized gradient approximation (GGA) and density functional theory (DFT). The valence electron-ion interaction was modeled using the projector augmented wave (PAW) potential model executed in the Vienna ab initio simulation package (VASP) [20-21]. For the results, the positions of all atoms and the lattice constant are relaxed until the force is less than 0.22 eV/Å. The total energy standard is 1×10^{-5} eV.

2.5. Photoelectrochemical measurements

In a normal three electrode system all electrochemical characterizations were tested, a synthetic photocatalyst as the working electrode, Ag/AgCl was used as the reference electrode, and platinum wire was employed as the counter electrode. The NaSO$_4$ solution of 0.5 M was chosen as electrolyte. The operating procedure of the working

electrode was as follows: 20 μL Naphthol and 4 mg sample were added into 1 mL

anhydrous ethanol, and the mixture was prepared by ultrasound for 30 min. Whereafter,

the compound was coated on the indiumtin oxide (ITO) glass. Then the photoanodes

with an area of 2.75 cm^2 were dried at 60°C for 8 h. The test light source was A 300 W

xenon lamp. By the Nernst equation: $E_{RHE} = E_{Ag/AgCl} + 0.197 + 0.059$ pH, the potential

measured was transformed into reverse hydrogen electrode (RHE). The chopped

illumination method was used to measure the transient photocurrents. The frequency

range of electrochemical impedance spectra (EIS) is $0.1\text{-}10^5$ Hz. polarization curve was

tested at 5 mVs^{-1} scan rate.

3. Results and discussion

3.1. Photocatalysts synthesis and characterization

In this work, as the cubic $BiO_{2\text{-}x}$ (BOv) lattice comprises a large quantity of oxygen

vacancies, it is represented as the model material for doping study. The X-ray diffraction

(XRD) spectrum (Fig. 1b) for Nd doped $BiO_{2\text{-}x}$ (BO_V:Nd) is corresponded with the

cubic BOv with space group of $Fm\bar{3}m$ relevantly (JCPDS: 47-1057), demonstrating that

Nd doping has not change the crystal phase. The Raman signals (Fig. S2) of BO_V and

BO_V:Nd give four same characteristic bands with BOv, indicating Nd atoms only exist

in doped modality. Then we employ energy-dispersive X-ray spectroscopy (EDS)

mapping on BO_V:Nd to confirm the doping of Nd element. As displayed in Fig. 1c, the

distribution of O, Bi, and Nd elements matching to the scanning transmission electron

microscopy (STEM) image reveals Nd doping. Inductively coupled plasma (ICP)

method was further performed to confirm the doping amount of Nd element, as shown

in Table S1. As shown in the results meeting with the added Nd precursor amount, the doped Nd can be skillfully controlled in the material syntheses. Transmission electron microscopy (TEM) (Fig. S3) highlights a characteristic of ultrathin nanosheets, which also can be affirmed by atomic force microscope (AFM), the average thickness of BO_V:Nd nanosheets is 1.45 nm, corresponding to one monolayer structure (Fig. 1d; see also Fig. S4).

In addition, aberration-corrected high-angle annular dark-field scanning transmission electron microscopy (HAADF-STEM) images (Fig. 1e and g) show up the atomic structure of the BO_V and BO_V:Nd. The interplanar spacing are measured 0.272 nm, which reveals the [200] orientation of the BO_V [22]. At the center of the nanosheet are uniformly distributed bright dot atoms. The configuration of atoms is determined by analyzing the line intensity profiles along the direction of the red dotted arrow. As shown, the line brightness level is symmetrical arrangement and the atomic brightness levels are comparable in Fig. 1f. Interestingly, it is noted that the corresponding line intensity decreases and low-brightness intensity of atoms appears along with the doping of the Nd atoms (Fig. 1h). The reason is that the atom column brightness in HAADF-STEM is related to the atomic number, and the brightness level should be Bi (83) > Nd (60) [23]. The doping of Nd does not change the lattice spacing, which is reflected in both HAADF-STEM images and intensity profile images. It can be concluded that the isolated Nd atoms substitute Bi atoms in the crystal lattice, which is further confirmed by the line intensity profile and selected-area intensity surface plot.

The surface chemical composition of the photocatalysts was recorded by the Fourier

transform infrared (FTIR) spectra (Fig. S5). In so far as BO_V, the characteristic absorption bands of the Bi-O bonds vibration in BiO_3 subuliform units appeared in FTIR spectra at 528 and 588 cm^{-1} [24]. Considering the structural characteristics of the BO_V, it essentially forms the low-valence Bi species and Bi-O-Bi interaction in the lattice. The binding energy of X-ray photoelectron spectroscopy (XPS) can reveal the valence states of elements in samples. The high-resolution Bi 4f XPS spectra of BO_V and BO_V:Nd (Fig. 2a) reveal that both Bi^{3+} species (binding energy at 158.2 and 163.5 eV) are existed in the samples, furthermore Bi^{5+} species (binding energy at 158.7 and 163.9 eV) for $4f_{7/2}$ and $4f_{5/2}$, respectively. And the similar results of BO_V and BO_V:Nd manifest that Nd doping does not alter the valence state of Bi. To explain the status of doped Nd, we tested a Nd 3d XPS spectrum for BO_V:Nd. Fig. 2b shows that the peak of Nd in Nd_2O_3 is located at 979.1 eV and Nd is coordinatively saturated, nevertheless, the peak of Nd 3d in BO_V:Nd is located at 976.9 eV, indicating the Nd is more likely to be coordinatively unsaturated [16]. Electron paramagnetic resonance (EPR) was noted to explore the generation of O vacancies, the results (Fig. 2c) show that the intensity of BO_V:Nd does not increase, which is consistent with the above conclusion.

Furthermore, the determination of Nd atom position in crystal lattice has been supported by our first-principles simulations, in which the Nd-doped BO_V with different doping configurations have different slab energies, as illustrated in Fig. 2d-g. Given that catalysis generally occurs on the surface of catalyst, various positions on the surface (Fig. 2d and e) or sub-surface (Fig. 2f and g) along the BO_V were investigated. The Nd atoms in Fig. 2d and f are far away from the oxygen vacancy, while in Fig. 2e

and g are connected to the oxygen vacancy. Of course, it needs more energy to replace the Bi on the sub-surface or far away from the oxygen vacancy. Based on all the above characterizations, it is proved that Nd atom replaces Bi atom connected by surface oxygen vacancy to form the unsaturated Nd-Bi dual-metal sites (Nd-Bi dual-metal sites).

3.2. Molecular Oxygen Activation Tests

Therein, the catalytic performance of the samples was systematically studied by taking O_2 activation experiment as an example. Meanwhile, the rate of TMB oxidation in nitrogen, air and oxygen conditions was tested under NIR irradiation, and the dramatically difference in the rate verify that the ROS formed from O_2 (Fig. 3a). In particular, the oxidation rate of modified samples in oxygen is 4.9 times that in nitrogen. For the sake of clarifying the type of ROS during TMB oxidation process, mannite, superoxide dismutase (SOD) and catalase were brought in the reaction system under NIR irradiation, which can specially restrain the generation of $\cdot OH$, $O_2^{\bullet-}$ and H_2O_2, respectively. Fig. 3b obviously shows that the TMB oxidation can be dramatically decreased by SOD, suggesting $O_2^{\bullet-}$ is the main photogenerated ROS. The same experiment under visible light shows that $O_2^{\bullet-}$ is the primary active species (see Fig. S7). Finally, to further examine the generation and intensity of ROS driven by irradiation, electron spin resonance (ESR) spectrum was also indicated. As illustrated in Fig. 3c, when 5,5-dimethyl-1-pyrroline-N-oxide (DMPO) is added to the reaction system, a signal associated with DMPO-OOH (a spin derivative of DMPO-$O_2^{\bullet-}$) is observed, proving the formation of $O_2^{\bullet-}$. Apparently, compared with BOv, BO_V:Nd exhibits a better ability for O_2 activation to $O_2^{\bullet-}$, and this conclusion was confirmed in

the $O_2^{\cdot-}$ quantitative experiments (see Fig. S8-9). Meanwhile, no significant $\cdot OH$ is generated in the activation process of O_2, further confirming BO_V:Nd exclusively generates $O_2^{\cdot-}$ (Fig. 3d). In conclusion, the Nd-Bi dual-metal sites in BO_V:Nd lead to high photocatalytic O_2 activation efficiency [25].

3.3. Mechanism of enhanced photocatalytic oxygen activation

In order to investigate the mechanism of the excellent photocatalytic performance of BO_V:Nd, its light absorption capacity and electron transmit capacity were studied. Firstly, the ultraviolet photoelectron spectroscopy (UPS) spectrum (Fig. 4a) suggests the metallic properties of BO_V and BO_V:Nd, which derived from the Bi 4f, O 1S, and Nd 3d with traversing the Fermi level (0 eV). For light absorption, the samples cover the UV, visible and near-infrared (NIR) light range (Fig. 4b). After doping Nd element, the absorption edge of the samples increases from 796 nm to 983 nm and the light absorption capacity is greatly enhanced. In the meantime the corresponding bandgap energies of BO_V and BO_V:Nd are 1.37 eV and 0.93 eV respectively, the calculation results are illustrated in Fig. 4b inset [26]. In addition, the Mott-Schottky plots of BO_V and BO_V:Nd were tested and are illustrated in Fig. 4c. The flat-band potentials of BO_V and BO_V:Nd are -0.31 and -0.28 eV, respectively. The conduction band potential (E_{CB}) is usually more negative (E = 0.1 - 0.3 V) than the flat band potential (E_{FB}) in n-type semiconductor. In this work, we choose E to be 0.1 V. To sum up, the E_{CB} potential of BO_V and BO_V:Nd are calculated to be -0.41 and -0.38 eV, satisfying the thermodynamic requirements for O_2 activation to yield $O_2^{\cdot-}$ (-0.33 eV), meanwhile the generation of $\cdot OH$ is not available, which is in line with the ESR results.

To uncover the effect of dual-metal sites on the electronic structures, the density functional theory (DFT) calculations were carried out. The density of states (DOS) through the Fermi level manifests the metallic behavior of BO_V and BO_V:Nd (Fig. 5a). The introduction of the Nd atom significantly enhances the DOS of valence band maximum (VBM), therefore, more electrons in BO_V:Nd can be photoexcited to conduction band under NIR light, promoting the electron transfer reactions and hence improving the O_2 activation [27]. Meanwhile, it can be understood from the high-resolution O 1s XPS spectra of BO_V and BO_V:Nd (Fig. S6) that the adsorption of O_2 on the modified photocatalyst surface increases, providing more advantageous conditions for the activation of O_2. When Nd replaced Bi nearby oxygen vacancy, the simulated charge distribution on the surface show that active site of BO_V:Nd gathers more electrons than BO_V (see the yellow cloud in Fig. 5b), thus offering theoretical basis of charge transfer and capture at Nd-Bi dual-metal sites directly [28]. And the calculated electronic band structures (Fig. 5c) reveal that the Nd doping can effectively shorten the BO_V band gap, which can be confirmed by the experimental results (Fig. 4b-c).

Besides, another factor that primarily affect the photochemical reaction, charge separation and transfer efficiency is worth researching. The charge separation extent and surface potential barrier of the excited state produced by absorption can be revealed from the surface photovoltage (SPV) spectroscopy. It is certified that the SPV spectroscopy generated by BO_V:Nd outdistances that of BO_V, with enhancement degree of over 10-fold in the range of 310-390 nm, revealing the more accelerated photocarriers separation efficiency. (Fig. 6a) [29]. This conclusion is supported by the

photocurrent response (Fig. 6c) and the photoluminescence (PL) spectroscopy (Fig. 6d). The higher photocurrent density and inferior PL emission peak of BO_V:Nd reveal the positive role of Nd doping for restraining the recombination of photocarriers, which should be contributed to that Nd-Bi dual-metal sites can play the part of electrons trap for accelerating the photocarriers separation. In addition, the charge transfer factor is surveyed by electrochemical impedance spectroscopy (EIS) spectroscopy (see Fig. 6b). The arc diameter can reflect the charge-transfer resistance. As compared, the diameter of BO_V is larger than that of BO_V:Nd, manifesting that the introduction of Nd-Bi dual-metal sites can reduce the interfacial charge transfer resistance, which is beneficial to photogenerated carriers transfer [10,30]. This conclusion is further supported by the time-resolved photoluminescence (TRPL) (Fig. 6e). As is known to that the possibility of all the charge carrier participation in photocatalytic reactions hinges on their lifetime prior to recombination [31]. Compared with BO_V, BO_V:Nd unfolds a longer intensity-average (τ) PL lifetime about 1.44 ns, indicating that more photogenerated electron-holes can be involved in the course of reaction, consistent with its fastest charge transfer rate. Meantime, to prove the increased electron transfer rate more strongly, linear sweep voltammetry (LSV) curves and open circuit potential (OCP) are also added to further illustrate. (Fig. S10-11). These results indicate that Nd substitution leads to significant charge separation and transfer of BO_V, which is responsible for the powerful molecular oxygen activation performance of Nd-Bi dual-metal sites.

3.4. Photocatalytic degradation of organic pollutants

During irradiation under visible light ($\lambda > 420$ nm) and NIR light ($\lambda > 800$ nm)

irradiation, respectively, a photolysis experiment of doxycycline (DC) was conducted to explore the catalytic activity of the generated ROS, where the respective contributions of ROS in the reactions were determined. The degradation of DC in the presence of BO_V and BO_V:Nd was also examined, respectively, for comparison. Compared to other techniques, high performance liquid chromatography offers many advantages, including good accuracy, specificity and precision. For that reason, a fast and straightforward way for DC is used in this paper, meanwhile the representative chromatogram and the standard curve of a standard solution of DC illuminated in Fig. S12 and S13. Then, the experimental parameters of degradation were determined by exploring the influence factors of catalyst dosage and initial concentration of DC (Fig. S14). The control experiment demonstrates that the adsorption saturation was reached after 10min in the dark, and the DC concentration did not decrease (Fig S15a). The improvement of adsorption effect may be due to the increase of BO_V:Nd specific surface area and the appearance of mesopore, which increases the adsorption site. This is also beneficial to the photocatalytic reaction (Fig. S16; Table S2). Experimental results show that 6% BO_V:Nd had the highest DC removal efficiency (86.14%), followed by 4% BO_V:Nd (70.54%), 8% BO_V:Nd (53.87%), 2% BO_V:Nd (50.51%), and BO_V sample (<10%) within 2 h under NIR irradiation (Fig. 7b). The DC degradation was accorded with the pseudo-first-order model commendably, meanwhile the kinetic constants (k) of degradation was 134.4×10^{-4} min^{-1} for BO_V:Nd, 24.2 times higher than BO_V for 5.56×10^{-4} min^{-1} (Fig. 7a). The results clearly suggest that BO_V:Nd has a relatively high photocatalytic capacity and could efficiently degrade organic

compounds such as DC under NIR light ($\lambda > 800$ nm) irradiation. Under the irradiation

of visible light, the catalyst degradation of tetracycline has the same effect, even within

1h can achieve the effect that BO_V:Nd had the highest DC removal efficiency (94.19%)

(Fig. 7d). The kinetic constants (k) of degradation was 410.1×10^{-4} min^{-1} for BO_V:Nd,

17.2 times higher than BO_V for 23.9×10^{-4} min^{-1} (Fig. 7c). The mineralization ability of

BO_V:Nd photocatalysts is ulteriorly demonstrated by TOC measurement. The TOC

removal rate of the BO_V:Nd reached about 72% under visible light irradiation for 60

min as illustrated in Fig. S15b. The consequence made clear the better photocatalytic

mineralization of BO_V:Nd for DC. More importantly, we found that the degradation of

DC by BO_V:Nd was largely ascribed to the photoinduced ROS, while $O_2^{\bullet-}$ played an

important part in the decomposition of DC.

To further quantify the contributions of various ROS to the degradation of DC, BQ

and IPA were used as quenching agents for $O_2^{\bullet-}$ and $\cdot OH$, respectively. BO_V:Nd was

selected as the most photoactive sample and used in this degradation experiment. It is

evident that the degradation of DC was substantially restrained after the addition of BQ

and slightly restrained after the addition of IPA (Fig. S17a) under NIR irradiation, which

evidenced the more important part of $O_2^{\bullet-}$ in the degradation of DC by BO_V and BO_V:Nd.

The same results can be obtained under visible light (Fig. S17b). It is well recognized

that $O_2^{\bullet-}$ is one of the most principal ROS toward organic compounds. Thus, it is likely

that $O_2^{\bullet-}$ primarily contributed to the photodegradation of DC in this study.

The intermediates were identified by using LC/MS to further understand the

decontamination process of BO_V:Nd for DC. The detailed LC-MS consequences are

exhibited in Fig. S18 and Table S3. As illustrated in Fig. 8a, two possible degradation routes are proposed. The primal signal of mass/charge is m/z = 461, which represents a complete structure parent DC molecule. Pathway I principally involve the separation of N-methyl and hydroxyl and the opening of benzene rings. Among them the intermediate DC1 (m/z = 475) generates DC2 (m/z = 434) through hydroxyl substitution reaction and N-C fracture, then DC2 loses hydroxyl and methyl, cracking the benzene ring and converting to substance DC3 (m/z = 207). At the same time, the midbody DC3 can be split into a smaller molecular DC4 (m/z = 149) [32]. Intermediates of pathway II are associated with progressive oxidation of reactive species. It can be seen from the LC-MS spectrum transformed by DC that $O_2^{\bullet-}$ attacked the C1 of benzene ring on DC, making the benzene ring open and resulting in larger molecules (m/z = 566). Subsequently, DC5 (m/z = 566) was decomposed to DC6 (m/z = 461) though demethylamine, dehydroxylation and oxidation. Under the action of $O_2^{\bullet-}$, DC6 (m/z = 461) was split into DC7 (m/z = 348) and DC8 (m/z = 185). These complex structures are further oxidized and step up to simpler organic compounds. Eventually these simple organic compounds like acids and alcohols will form water and carbon dioxide [33-34].

In order to analyze and predict the toxicity of DC and the degradation products in the photocatalytic process toward aquatic creatures, the chronic and acute toxicities were figured up by using EPI Suite software at three trophic levels. As shown in Fig. 7b, the acute toxicity was reckoned as LC_{50} for fish and daphnia, and EC_{50} for green algae, and these results were 24.3×10^6, 1.32×10^5, and 5.16×10^5 mg/L for DC, respectively. Meanwhile the chronic toxicity values (ChVs) of DC were 1.55×10^6, 5.06×10^3, and

9.73×10^4 mg/L for three aquatic organisms respectively. The result attests that DC is not detrimental to aquatic creatures on account of European Union criteria and Chinese hazard evaluation guidelines for new chemical substances (HJ/T 154-2004). Except for DC3 and DC6 to daphnia for the acute toxicities of intermediate products, most middle products had non noxious to fish, daphnia, and green algae. So, these hazardous intermediate products would be generated during the photocatalytic degradation of DC employing the BO_V:Nd catalyst. But these intermediates could be ulteriorly detoxified by active species via degrading and converting to H_2O and CO_2 in plenty of time, demonstrating the BO_V:Nd catalyst is quite effective in degrading DC [35]. The experimental results under the same conditions show that the BO_V:Nd composite has remarkable DC degradation capabilities as compared with state-of-the-art materials by near infrared light (reference in the degradation system of antibiotic pollutants in the existing literature to prepare catalyst), as shown in Fig. 8c [36-41].

To verify the efficiency of catalyst, apart from DC, the degradation of sodium butyl xanthate in mineral processing wastewater and related experiments were carried out, the experimental results can be sought in the support information (see Fig. S19-23). To investigate the stability of BO_V:Nd composite, five recycling experiment of BO_V:Nd sample was carried out. It is distinct that the activity of BO_V:Nd composite is reduced fractionally after five cycles under light irradiation (Fig. S24a). This could be a loss of catalyst during the cycle. Anyway, the composite still maintained a high photocatalytic activity after five cycles. At the same time, the XRD and XPS spectra of the catalyst changed negligible compared with that of the fresh catalyst (Fig. S24b and S25)

confirms the robust photostability of BO_V:Nd composites. The remarkable result is that the DC degradation situation maintains unchanged with increasing typical background matters in water incorporating OA, CA, HCO_3^- and Cl^- (Fig. S26), also in tap water and river water (Xi Lake, Hebei University of Technology, Fig. S27). Hence, the unsaturated Nd-Bi dual-metal sites catalyst has good environmental stability and is a promising tactics for down-to-earth application.

4. Conclusions

In conclusion, using Nd-doped BiO_{2-x} with abundant surface oxygen vacancies as a research object, we have certified that unsaturated Nd-Bi dual-metal sites can drive surface O_2 chemisorption and promote charge separation and transfer, leading to high-efficiency photocatalytic O_2 activation under NIR light. Theoretical and characterization analysis prove that Nd substitution induce unsaturated dual-metal sites, resulting a high charge-separation efficiency, and promote their transferring from the principal part to the surface. Surface O vacancy can reduce the conduction band, serving as the active sites for chemisorbing O_2 molecules and capturing electrons from the principal part. Moreover, only substitution nearby the surface O vacancies can achieve this effect. Because plentiful electrons can migrate to the surface, surface O vacancies can effectually transmit electrons to the chemisorbed O_2, leading the O_2 activation to $O_2^{\bullet-}$ rapidly. Profiting from multitude $O_2^{\bullet-}$ generation, the Nd doped half-metal BiO_{2-x} is represented to manifest outstanding performance for photocatalytic degradation. This work makes contribution to charge transfer and surface O_2 activization synchronously, and aggrandizes the cognition related to unsaturated dual-metal sites in catalysis

process.

Credit authorship contribution statement

Qiuwen Wang: Investigation, Writing - Original Draft and Formal analysis; Dongyu Xu: Writing - Review & Editing; Yilin Dong: Validation; Shaoxuan Pang: Investigation; Lijun Zhang: Conceptualization; Guangming Zhang: Supervision; Longyi Lv: Investigation; Xiaoyang Liu: Validation; Yuguo Xia: Software; Luiza C Campos: Validation; Zhijun Ren: Supervision and Funding acquisition; Pengfei Wang: Supervision, Funding acquisition and Writing - Review & Editing.

Competing interest

The authors declare no competing interests.

Acknowledgements

References:

[1] J. Jiang, X. Wang, Y. Liu, Y. Ma, T. Li, Y. Lin, T. Xie, S. Dong, Photo-Fenton degradation of emerging pollutants over Fe-POM nanoparticle/porous and ultrathin g-C_3N_4 nanosheet with rich nitrogen defect: Degradation mechanism, pathways, and products toxicity assessment, Appl. Catal. B: Environ. 278 (2020) 119349. https://doi.org/10.1016/j.apcatb.2020.119349

[2] S. Liu, P. Wang, C. Wang, J. Chen, X. Wang, B. Hu, Q. Yuan, Ecological insights into the disturbances in bacterioplankton communities due to emerging organic pollutants from different anthropogenic activities along an urban river, Sci Total Environ. 796 (2021) 148973. https://doi.org/10.1016/j.scitotenv.2021.148973

[3] S. Zainab, M. Junaid, N. Xu, R. Malik, Antibiotics and antibiotic resistant genes (ARGs) in groundwater: A global review on dissemination, sources, interactions, environmental and human health risks, Water Res. 178 (2020) 116455. https://doi.org/10.1016/j.watres.2020.116455

[4] M. Barbosa, N. Moreira, A. Ribeiro, M. Pereira, A. Silva, Occurrence and removal of organic micropollutants: An overview of the watch list of EU Decision, Water Res. 94 (2016) 257-279. https://doi.org/10.1016/j.watres.2016.02.047

[5] D. Miklos, C. Remy, M. Jekel, K. Linden, J. Drewes, U. Hubner, Evaluation of advanced oxidation processes for water and wastewater treatment-A critical review, Water Res. 139 (2018) 118-131. https://doi.org/10.1016/j.watres.2018.03.042

[6] X. Du, W. Fu, P. Su, J. Cai, M. Zhou, Internal-micro-electrolysis-enhanced heterogeneous electro-Fenton process catalyzed by $Fe/Fe_3 C@PC$ core-shell hybrid for sulfamethazine degradation, Chem. Eng. J. 398 (2020) 125681. https://doi.org/10.1016/j.cej.2020.125681

[7] X. Sun, X. Luo, X. Zhang, J. Xie, S. Jin, H. Wang, X. Zheng, X. Wu, Y. Xie, Enhanced Superoxide Generation on Defective Surfaces for Selective Photooxidation, J. Am. Chem. Soc. 141 (2019) 3797-3801. https://doi.org/10.1021/jacs.8b13051

[8] Q. Zhou, S. Ma, S. Zhan, Superior photocatalytic disinfection of Ag-3D ordered mesoporous CeO_2 under visible light condition, Appl. Catal. B: Environ. 224 (2018) 27-37. https://doi.org/10.1016/j.apcatb.2017.10.032

[9] Q. Zhou, X. Hu, Systemic stress and recovery patterns of rice roots in response to

graphene oxide nanosheets, Environ. Sci. Technol. 51 (2017) 2022-2030. https://doi.org/10.1021/acs.est.6b05591

[10] P. Wang, Y. Mao, L. Li, Z. Shen, X. Luo, K. Wu, P. An, H. Wang, L. Su, Y. Li, S. Zhan, Unraveling the Interfacial Charge Migration Pathway at the Atomic Level in a Highly Efficient Z-Scheme Photocatalyst, Angew. Chem. Int. Ed. 58 (2019) 11329-11334. https://doi.org/10.1002/anie.201904571

[11] J. Li, W. Pan, Q. Liu, Z. Chen, Z. Chen, X. Feng, H. Chen, Interfacial Engineering of $Bi_{19}Br_3S_{27}$ Nanowires Promotes Metallic Photocatalytic CO_2 Reduction Activity under Near-Infrared Light Irradiation, J. Am. Chem. Soc. 143 (2021) 6551-6559. https://doi.org/10.1021/jacs.1c01109

[12] P. Riente, M. Fianchini, P. Llanes, M. Pericàs, T. Noël, Shedding light on the nature of the catalytically active species in photocatalytic reactions using Bi_2O_3 semiconductor, Nat. Commun. 12 (2021) 625. https://doi.org/10.1038/s41467-020- 20882-x

[13] X. Gao, Y. Shang, L. Liu, F. Fu, Chemisorption-enhanced photocatalytic nitrogen fixation via 2D ultrathin p-n heterojunction $AgCl/\delta$-Bi_2O_3 nanosheets, J. Catal. 371 (2019) 71-80. https://doi.org/10.1016/j.jcat.2019.01.002

[14] Y. Lin, S. Wu, X. Li, X. Wu, C. Yang, G. Zeng, Y. Peng, Q. Zhou, L. Lu, Microstructure and performance of Z-scheme photocatalyst of silver phosphate modified by MWCNTs and Cr-doped $SrTiO_3$ for malachite green degradation, Appl. Catal. B: Environ. 227 (2018) 557-570. https://doi.org/10.1016/j.apcatb.2018.01.054

[15] T. Zhang, M. Wu, D. Yan, J. Mao, H. Liu, W. Hu, X. Du, T. Ling, S. Qiao, Engineering oxygen vacancy on NiO nanorod arrays for alkaline hydrogen evolution, Nano Energy. 43 (2018) 103-09. https://doi.org/10.1016/j.nanoen.2017.11.015

[16] N. Zhang, A. Jalil, D. Wu, S. Chen, Y. Liu, C. Gao, W. Ye, Z. Qi, H. Ju, C. Wang, X. Wu, L. Song, J. Zhu, Y. Xiong, Refining Defect States in $W_{18}O_{49}$ by Mo Doping: A

Strategy for Tuning N_2 Activation towards Solar-Driven Nitrogen Fixation, J. Am. Chem. Soc. 140 (2018) 9434-9443. https://doi.org/10.1021/jacs.8b02076

[17] J. Li, J. Wang, G. Zhang, Y. Li, K. Wang, Enhanced molecular oxygen activation of Ni^{2+}-doped BiO_{2-x} nanosheets under UV, visible and near-infrared irradiation: Mechanism and DFT study, Appl. Catal. B: Environ. 234 (2018) 167-177. https://doi.org/10.1016/j.apcatb.2018.04.016

[18] A. Nagendrakumar, UV Assay method for the determination of Doxycycline Hyclate in Bulk and Pharmaceutical Formulation, Chem. Sci. Trans. 4 (2015) 69-74. https://www.researchgate.net/publication/291229503

[19] X. Zhou, A. Jawad, M. Luo, C. Luo, T. Zhang, H. Wang, J. Wang, S. Wang, Z. Chen, Z. Chen, Regulating activation pathway of Cu/persulfate through the incorporation of unreducible metal oxides: Pivotal role of surface oxygen vacancies, Appl. Catal. B: Environ. 286 (2021) 119914. https://doi.org/10.1016/j.apcatb.2021.119914

[20] G. Kresse, J. Hafner, Ab initio molecular dynamics for liquid metals, Phys. Rev. B. 47 (1993) 558. https://doi.org/10.1103/PhysRevB.47.558

[21] G. Kresse, J. Furthmiiller, Efficiency of ab-initio total energy calculations for metals and semiconductors using a plane-wave basis set, Comput. Mater. Sci. 6 (1996) 15-50. https://doi.org/10.1016/0927-0256(96)00008-0

[22] J. Li, X. Wu, W. Pan, G. Zhang, H. Chen, Vacancy-Rich Monolayer BiO_{2-x} as a Highly Efficient UV, Visible, and Near-Infrared Responsive Photocatalyst. Angew. Chem. Int. Ed. 57 (2018) 491-495. https://doi.org/10.1002/anie.201708709

[23] Z. Zhu, Y. Qu, Z. Wang, F. Zhou, C. Zhao, Y Lin, L. Li, Y. Yao, Y. Wu, 2D PbS Nanosheets with Zigzag Edges for Efficient CO_2 Photoconversion, Chem. Eur. J. 26 (2020) 13601-13605. https://doi.org/10.1002/chem.202001863

[24] J. Wang, Z. Liu, Z. Liu, $BiO_{2-x}/NaBiO_3$ hybrid composites: Facile synthesis, enhanced photocatalytic activity and mechanism, Solid State Sci. 95 (2019) 105935. https://doi.org/10.1016/j.solidstatesciences.2019.105935

[25] X. Song, G. Qin, G. Cheng, W. Jiang, X. Chen, W. Dai, X. Fu, Oxygen defect induced NO^- intermediates promoting NO deep oxidation over Ce doped SnO_2 under visible light, Appl. Catal. B: Environ. 284 (2021) 119761. https://doi.org/10.1016/j.apcatb.2020.119761

[26] G. Cheng, X. Liu, X. Song, X. Chen, W. Dai, R. Yuan, X. Fu, Visible-light-driven deep oxidation of NO over Fe doped TiO_2 catalyst: Synergic effect of Fe and oxygen vacancies, Appl. Catal. B: Environ. 277 (2020) 119196. https://doi.org/10.1016/j.apcatb.2020.119196

[27] P. Wang, Z. Shen, Y. Xia, H. Wang, L. Zheng, W. Xi, S. Zhan. Atomic insights for optimum and excess doping in photocatalysis: A case study of few-layer $Cu-ZnIn_2S_4$, Adv. Funct. Mater. 29 (2019) 1807013. https://doi.org/10.1002/adfm.201807013

[28] Y. Mao, P. Wang, L. Li, Z. Chen, H. Wang, Y. Li, S. Zhan, Unravelling the Synergy between Oxygen Vacancy and Oxygen Substitution in BiO_{2-x} for Efficient Molecular Oxygen Activation, Angew. Chem. Int. Ed. 132 (2019) 3714-3719. http:// dx.doi.org/ 10.1002/ange.201914001

[29] H. Huang, S. Tu, C. Zeng, T. Zhang, A. Reshak, Y. Zhang, Macroscopic polarization enhancement promoting photo-and piezoelectric-induced charge separation and molecular oxygen activation, Angew. Chem. Int. Ed. 129 (2017) 12022-12026. https://doi.org/10.1002/ange.201706549

[30] X. Song, W. Jiang, Z. Cai, X. Yue, X. Chen, W. Dai, X. Fu, Visible light-driven deep oxidation of NO and its durability over Fe doped $BaSnO_3$: The NO^+ intermediates mechanism and the storage capacity of Ba ions, Chem. Eng. J. 444 (2022) 136709.

https://doi.org/10.1016/j.cej.2022.136709

[31] X. Wang, X. Wang, J. Huang, S. Li, A. Meng, Z. Li, Interfacial chemical bond and internal electric field modulated Z-scheme $Sv\text{-}ZnIn_2S_4/MoSe_2$ photocatalyst for efficient hydrogen evolution, Nat Commun. 12 (2021) 1-11. https://doi.org/10.1038/s41467-021-24511-z

[32] H. Wang, B. Liao, T. Lu, Y. Ai, G. Liu, Enhanced visible-light photocatalytic degradation of tetracycline by a novel hollow $BiOCl@CeO_2$ heterostructured microspheres: Structural characterization and reaction mechanism, J. Hazard. Mater. 385 (2020) 121552. https://doi.org/10.1016/j.jhazmat.2019.121552

[33] X. Yan, J. Qian, X. Pei, L. Zhou, R. Ma, M. Zhang, Y. Du, L. Bai, Enhanced photodegradation of doxycycline (DOX) in the sustainable $NiFe_2O_4/MWCNTs/BiOI$ system under UV light irradiation, Environ. Res. 199 (2021) 111264. https://doi.org/10.1016/j.envres.2021.111264

[34] P. Ganguly, S. Mathew, L. Clarizia, S. Kumar R, A. Akande, S. Hinder, A. Breen, S.C. Pillai, Theoretical and experimental investigation of visible light responsive $AgBiS_2\text{-}TiO_2$ heterojunctions for enhanced photocatalytic applications, Appl. Catal. B: Environ. 253 (2019) 401-418. https://doi.org/10.1016/j.apcatb.2019.04.033

[35] X. Nie, G. Li, S. Li, Y. Luo, W. Luo, Q. Wan, T. An, Highly efficient adsorption and catalytic degradation of ciprofloxacin by a novel heterogeneous Fenton catalyst of hexapod-like pyrite nanosheets mineral clusters, Appl. Catal. B: Environ. 300 (2022) 120734. https://doi.org/10.1016/j.apcatb.2021.120734

[36] J. Liu, S. Guo, H. Wu, X. Zhang, J. Li, K. Zhou, Synergetic effects of Bi^{5+} and oxygen vacancies in Bismuth(V)-rich Bi_4O_7 nanosheets for enhanced near-infrared light driven photocatalysis, J. Mate. Sci. Technol. 85 (2021) 1-10. https://doi.org/10.1016/j.jmst.2021.01.022

[37] M. Mohebinia, C. Wu, G. Yang, S. Dai, A. Hakimian, T. Tong, H. Ghasemi, Z. Wang, D. Wang, Z. Ren, J. Bao, Ultrathin bismuth oxyiodide nanosheets for photocatalytic ammonia generation from nitrogen and water under visible to near-infrared light, Mater. Today. Phys. 16 (2021) 100293. https://doi.org/10.1016/j.mtphys.2020.100293

[38] Y. Yang, X. Zhang, C. Niu, H. Feng, P. Qin, H. Guo, C. Liang, L. Zhang, H. Liu, L. Li, Dual-channel charges transfer strategy with synergistic effect of Z-scheme heterojunction and LSPR effect for enhanced quasi-full-spectrum photocatalytic bacterial inactivation: new insight into interfacial charge transfer and molecular oxygen activation, Appl. Catal. B: Environ. 264 (2020) 118465. https://doi.org/10.1016/j.apcatb.2019.118465

[39] Y. Deng, L. Tang, C. Feng, G. Zeng, Z. Chen, J. Wang, H. Feng, B. Peng, Y. Liu, Y. Zhou, Insight into the dual-channel charge-charrier transfer path for nonmetal plasmonic tungsten oxide based composites with boosted photocatalytic activity under full-spectrum light. Appl. Catal. B: Environ. 235 (2018) 225-237. https://doi.org/10.1016/j.apcatb.2018.04.075

[40] B. Xiao, W. Zhao, Y. Xiang, X. Wu, G. Zhang, Vis-NIR responsive $Bi_{24}O_{31}Br_{10}$ and corresponding composite with up-conversion phosphor towards efficient photocatalytic oxidation, Appl. Surf. Sci. 489 (2019) 210-219. https://doi.org/10.1016/j.apsusc.2019.05.355

[41] Y. Wang, Q. Liu, N. Wong, J. Sunarso, J. Huang, G. Dai, X. Hou, X. Li, Near-infrared (NIR) light responsiveness of $CuS/S-C_3N_4$ heterojunction photocatalyst with enhanced tetracycline degradation activity, Ceram. Int. 48 (2022) 2459-2469. https://doi.org/10.1016/j.ceramint.2021.10.027

Figure captions
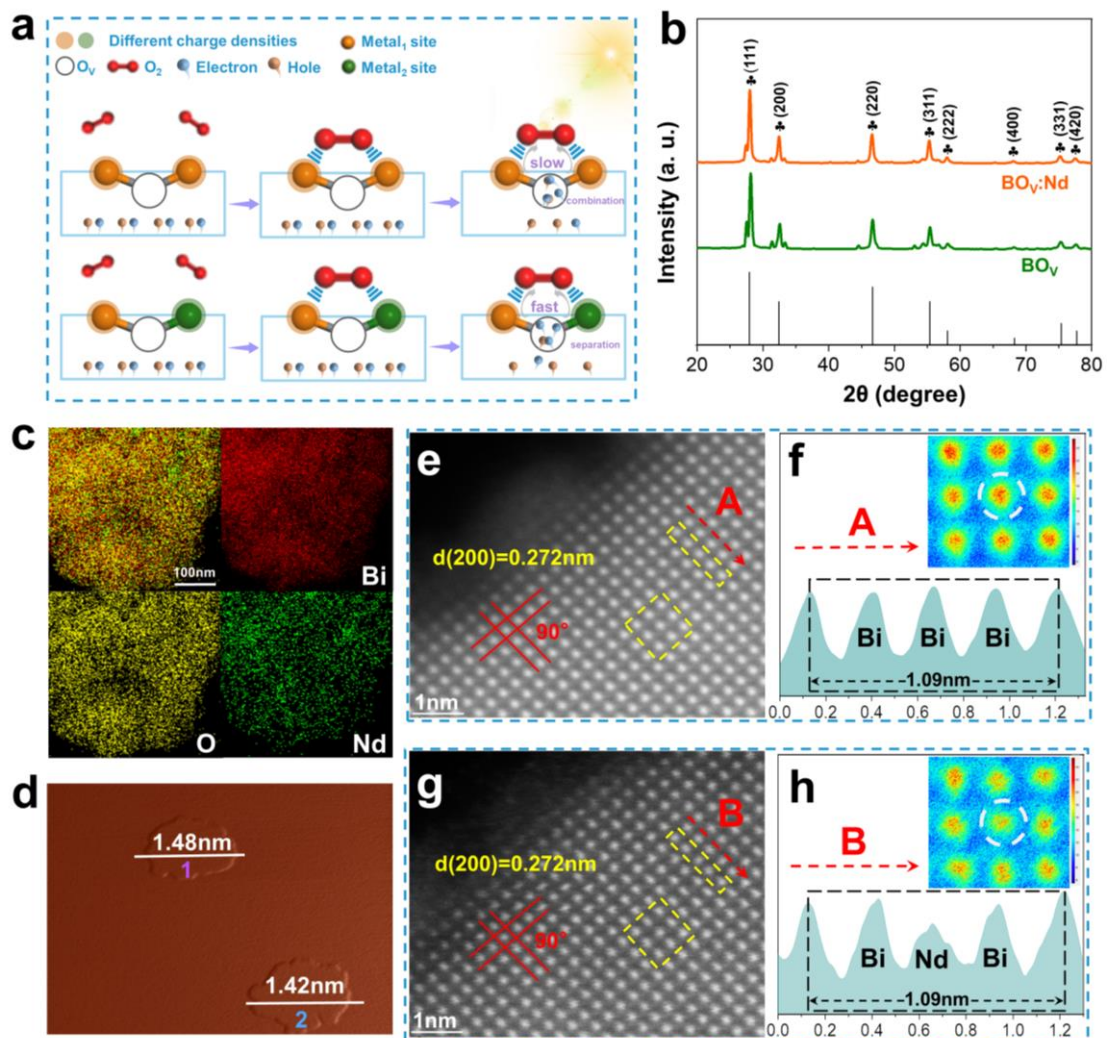
Fig. 1. (a) Schematic diagram of electron transfer at bimetallic sites. (b) XRD spectra of BO$_V$ and BO$_V$:Nd. (c) EDS elemental mapping profiles of BO$_V$:Nd. (d) AFM image of BO$_V$:Nd. (e and g) HAADF-STEM images of BO$_V$:Nd. (f and h) intensity profile corresponding to the yellow and red dotted arrow in HAADF-STEM images, respectively.
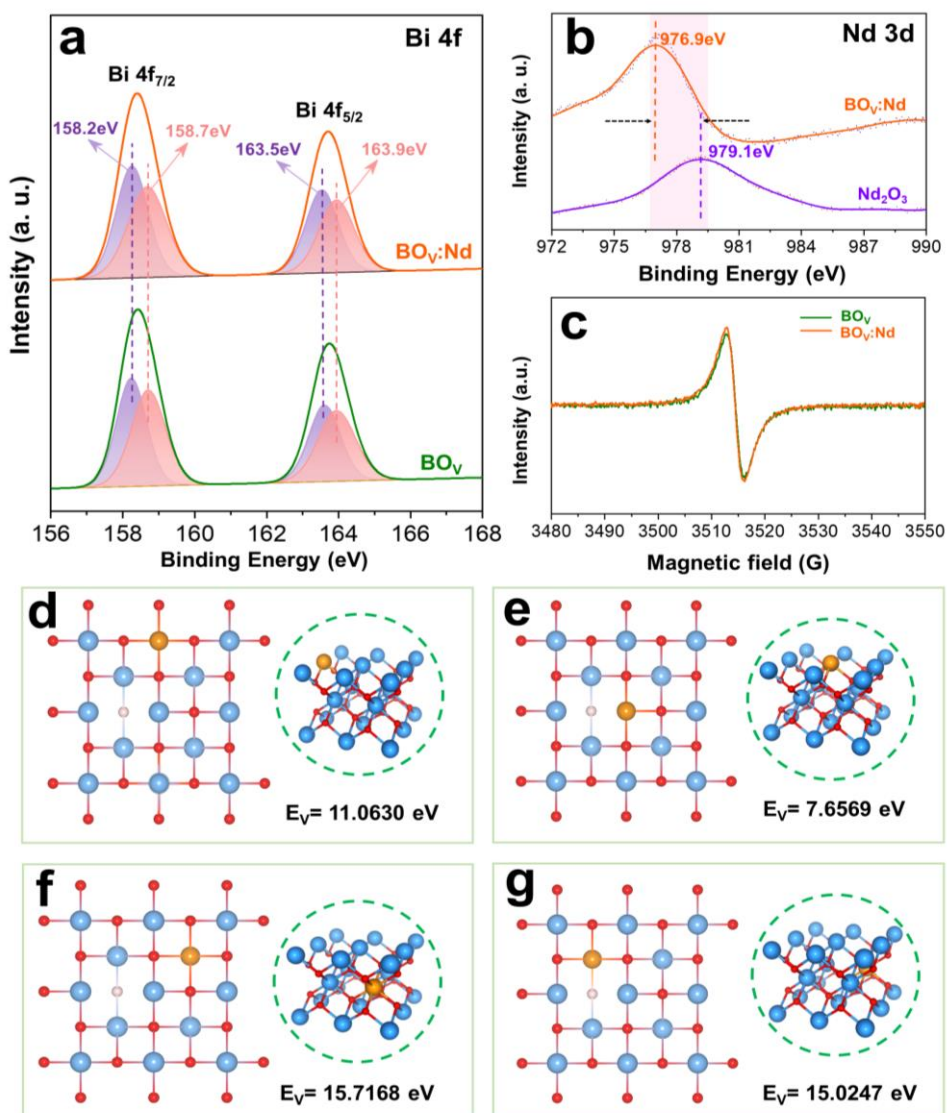
**Fig. 2.** High-resolution XPS spectra of the samples: (a) Bi 4f and (b) Nd 3d of BO_V and BO_V:Nd samples. (c) EPR spectra of DMPO-$O_2^{•-}$ obtained from BO_V and BO_V:Nd samples. (d-g) Possible sites of Nd doping to replace Bi atom and the corresponding slab energies of Nd-doped models calculated by first-principles simulations.
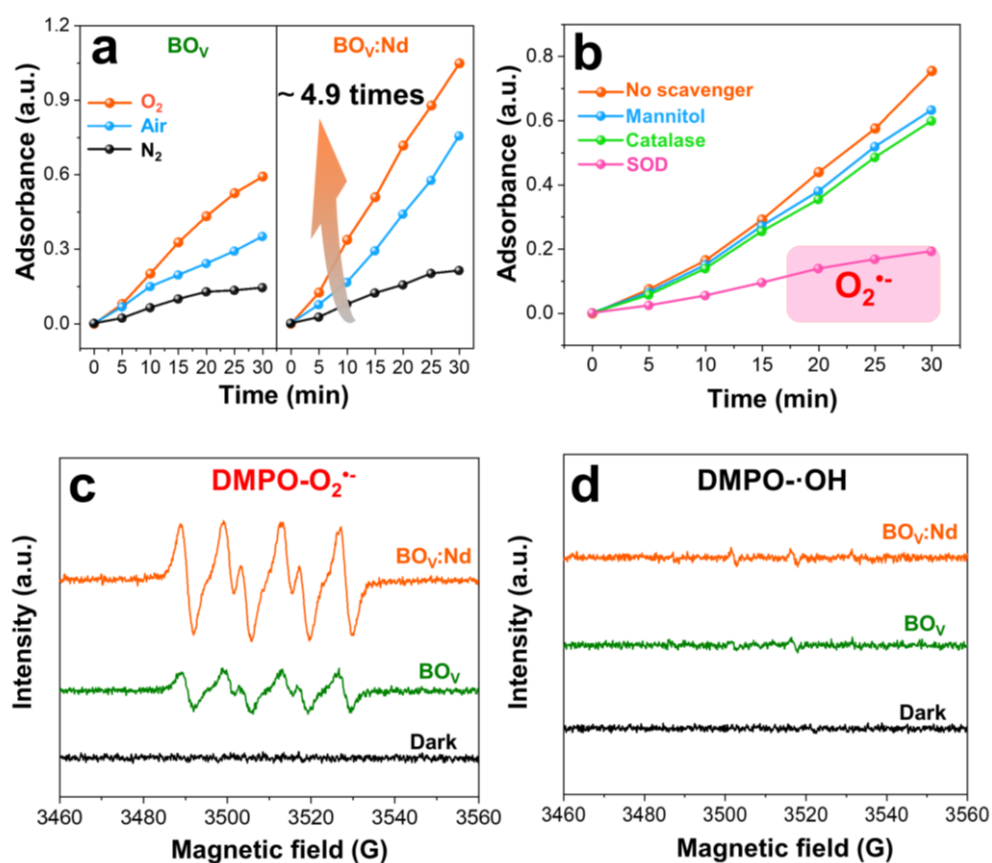
Fig. 3. (a) The absorbance peak vs reaction time under different gas conditions of BOv and BO_V:Nd under NIR light irradiation at 370 nm. (b) Absorbance change over BO_V:Nd with different scavengers of TMB oxidation under NIR light irradiation. (c) ESR spectra of BO_V and BO_V:Nd under DMPO for $O_2^{•-}$. (d) ESR spectra of BO_V and

BO$_V$:Nd under DMPO for ·OH.
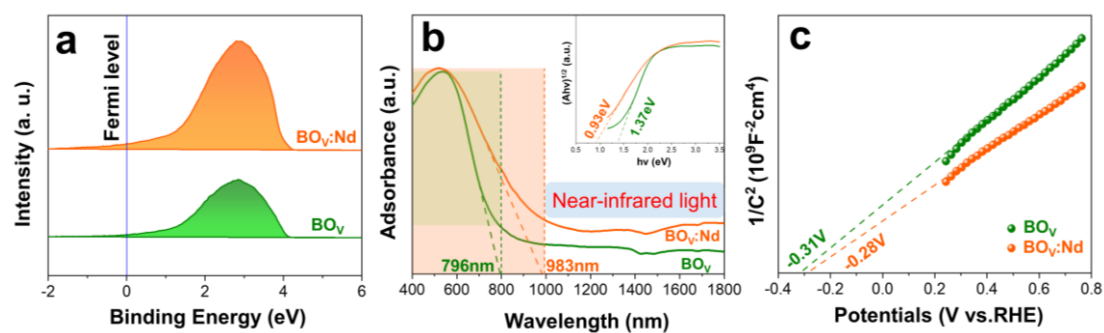
Fig. 4. (a) UPS spectra of BOv and BO$_V$:Nd. (b) UV/Vis-NIR diffuse reflectance spectra of BO$_V$ and BO$_V$:Nd with the inset showing the band gap energy (Eg) of BO$_V$ and BO$_V$:Nd. (c) Mott-Schottky spectra of BOv and BO$_V$:Nd.
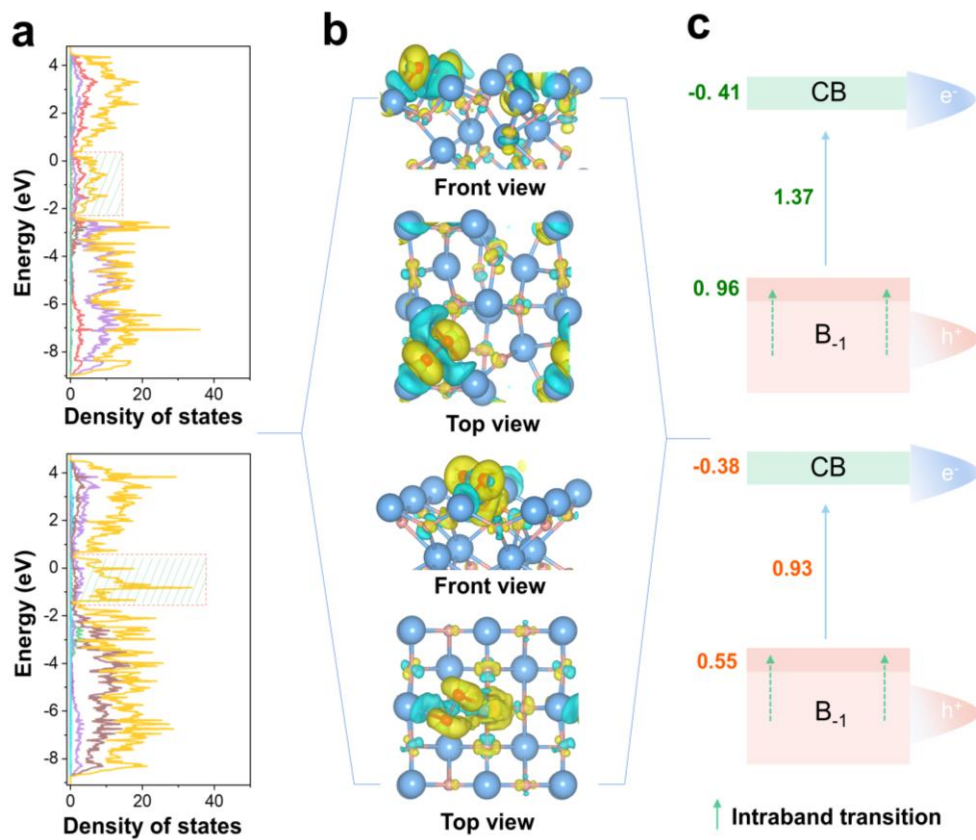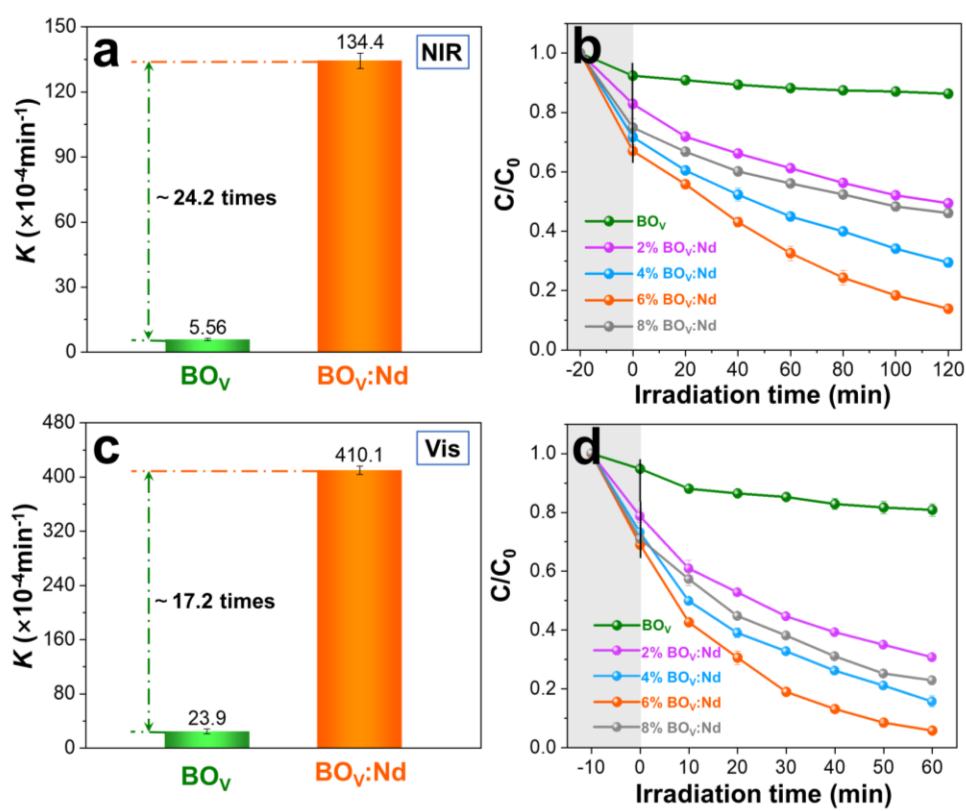
Fig. 5. (a) State density of BO_V and BO_V:Nd. (b) Differential charge density of BO_V and BO_V:Nd after oxygen adsorption. (c) Schematic diagram for the band alignments of BO_V and BO_V:Nd.
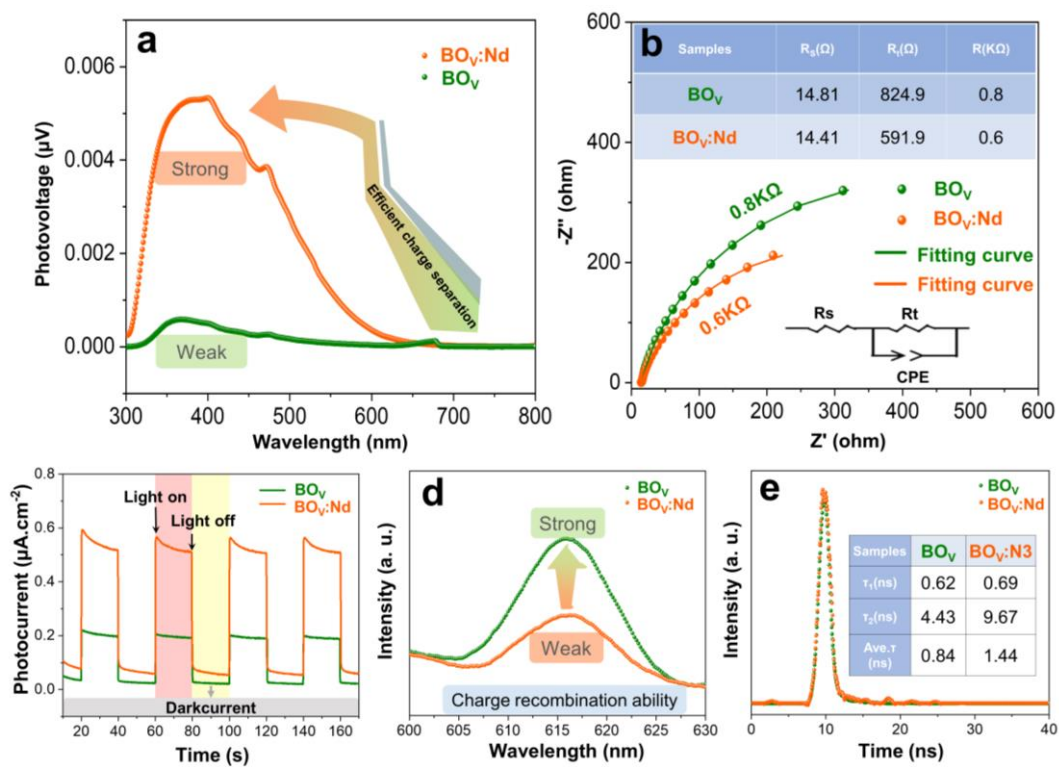
Fig. 6. (a) SPV plots of BO$_V$ and BO$_V$:Nd. (b) EIS Nyquist plots of BO$_V$ and BO$_V$:Nd.

(c) Transient photocurrent responses of BO$_V$ and BO$_V$:Nd. (d) PL spectra of BO$_V$ and

BO$_V$:Nd. (e) TRPL decay spectra of BO$_V$ and BO$_V$:Nd.

Fig. 7. Reaction-rate constant for DC degradation over BO_V and BO_V:Nd under (a) NIR light ($\lambda > 800$ nm) and (c) visible light ($\lambda > 420$ nm). Photocatalytic degradation of DC under (b) NIR light ($\lambda > 800$ nm) and (d) visible light ($\lambda > 420$ nm).
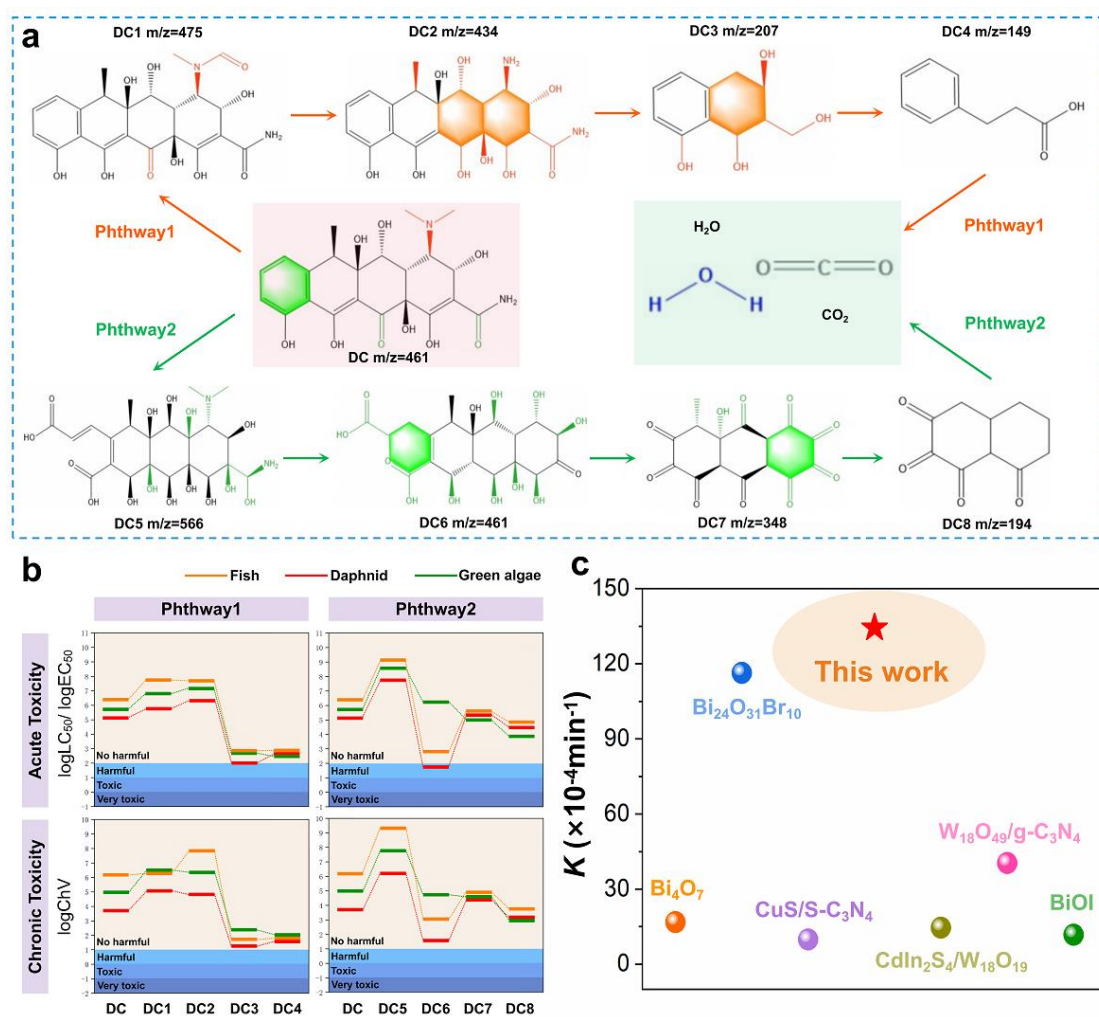
Fig. 8. (a) The possible degradation pathway of DC by the BO$_V$:Nd. (b) Acute and chronic toxicity evolution of DC and the degradation intermediates to three aquatic organisms. (c) comparison of the kinetic constants (k) of degradation previously reported in the degradation system of DC by near infrared light with this work.